For correspondence
Name: Kensuke Nishioka
Address: Japan Advanced Institute of Science and Technology, 1-1 Asahidai, Nomi, Ishikawa 923-1292, Japan
Tel/Fax/E-mail: +81-761-51-1562 / +81-761-51-1149 / nishioka@jaist.ac.jp

Evaluation of InGaP/InGaAs/Ge Triple-Junction Solar Cell and Optimization of Solar Cell's Structure Focusing on Series Resistance for High-Efficiency Concentrator Photovoltaic Systems

Kensuke Nishioka[1], Tatsuya Takamoto[2], Takaaki Agui[2], Minoru Kaneiwa[2], Yukiharu Uraoka[3] and Takashi Fuyuki[3]

[1]Graduate School of Materials Science, Japan Advanced Institute of Science and Technology
1-1 Asahidai, Nomi, Ishikawa, 923-1292, Japan
[2]SHARP Corporation
282-1 Hajikami, Shinjo-cho, Kitakatsuragi-gun, Nara 639-2198, Japan
[3]Graduate School of Materials Science, Nara Institute of Science and Technology
8916-5 Takayama, Ikoma, Nara 630-0101, Japan

ABSTRACT

The series resistance of an InGaP/InGaAs/Ge triple-junction solar cell was evaluated in detail. Series resistance components such as electrode resistance, tunnel junction resistance and lateral resistance between electrodes were estimated separately. The characteristics of the triple-junction solar cell under concentrated light were evaluated by equivalent circuit calculation with a simulation program with integrated circuit emphasis (SPICE). By equivalent circuit calculation, the optimization of cell designs was performed, focusing on series resistance and cell current in order to realize high-efficiency concentrator cells.

KEYWORDS: Triple-junction solar cell, Series resistance, Circuit calculation, Concentrated light, SPICE

1. INTRODUCTION

Multijunction solar cells consisting of InGaP, (In)GaAs and Ge are known to have an ultrahigh efficiency and are now used for space applications. The multijunction solar cells lattice-matched to Ge substrates have been improved and their conversion efficiency has reached 31% (AM1.5G) due to the lattice-matched configuration [1, 2].

A concentrator photovoltaic (PV) system using high-efficiency solar cells is one of the important issues for the development of an advanced PV system. The production cost of multijunction solar cells composed of III-V materials is higher than that of Si solar cells. However, the necessary cell size decreases with increasing concentration ratio, and the total cost of concentrator systems decreases. High-efficiency multijunction solar cells for high-concentration operation have been investigated for terrestrial applications [3, 4]. Also, for low-concentration operation, multijunction solar cells have been investigated for space satellite use [5-7].

However, energy losses due to the series resistance caused by the handling of large currents decrease the conversion efficiency of solar cells [8, 9]. The power loss resulting from series resistance (R_s) is expressed by the multiplication of the second power of current and series resistance ($I^2 R_s$). R_s becomes a dominant factor of cell efficiency with increasing current. Therefore, solar cells for concentrator applications must be carefully designed to minimize such losses.

In this study, the R_s of a triple-junction solar cell has been evaluated in detail. Moreover, the optimization of cell designs by calculation with a simulation program with integrated circuit emphasis (SPICE) has been performed, focusing on R_s and cell current in order to realize high-efficiency concentrator cells.

2. SAMPLE PREPARATION

Figure 1 shows a schematic of the InGaP/InGaAs/Ge triple-junction solar cell evaluated in this study. The subcells (InGaP, InGaAs and Ge junctions) of the triple-junction solar cell were grown on a *p*-type Ge substrate by metal-organic chemical vapor deposition. The $In_{0.49}Ga_{0.51}P$ top, $In_{0.01}Ga_{0.99}As$ middle, and Ge bottom subcells were all lattice-matched. The InGaP subcell was connected to the InGaAs subcell by a *p*-AlGaAs/*n*-InGaP tunnel junction. The InGaAs subcell was connected to the Ge subcell by a *p*-GaAs/*n*-GaAs tunnel junction.

Figure 2 shows the measured spectral response (external quantum efficiency (EQE)) of the InGaP/InGaAs/Ge triple-junction solar cell. As shown in Fig. 2, the InGaP/InGaAs/Ge triple-junction solar cell can absorb light of a wide wavelength and convert it into electricity.

The InGaP/InGaAs/Ge triple-junction solar cell is fabricated by connecting three subcells in series. Therefore, the open-circuit voltage (V_{oc}) of the triple-junction cell is the sum of the photovoltages from three subcells, and the short-circuit current (I_{sc}) is limited by the smallest subcell photocurrent. The photocurrents from InGaP, InGaAs and Ge subcells for 1 sun (100 mW/cm^2, AM1.5G) are designed to be 13.78, 15.74 and 20.60 mA/cm^2, respectively. Therefore, the I_{sc} of the InGaP/InGaAs/Ge triple-junction solar cell is limited by the photocurrent from the InGaP subcell, and the sufficient margin for the photocurrent from the Ge subcell is given.

Figure 3 shows a schematic of the upper electrode configuration of the InGaP/InGaAs/Ge triple-junction solar cell. The electrodes were fabricated by evaporation. The electrode consists of a 5-μm-thick Ag. The width and pitch of grid electrodes were 7 μm and 120 μm, respectively. The number of grid electrodes was 55.

3. SERIES RESISTANCE OF TRIPLE-JUNCTION SOLAR CELL

3.1 Measurement of series resistance

The current-voltage (*I-V*) characteristics of solar cells are given by

$$I = I_0\left\{\exp\left(\frac{qV}{nkT}\right)-1\right\}-I_{sc}, \qquad (1)$$

where I_0, q, n, k, and T are the saturation current, elementary charge, diode ideality factor, Boltzmann constant and absolute temperature, respectively. If shunt resistance (R_{sh}) is sufficiently large to be neglected, the *I-V* characteristics of the solar cells including series resistance (R_s) are given by

$$I = I_0\left\{\exp\left(\frac{q(V-IR_s)}{nkT}\right)-1\right\}-I_{sc}. \qquad (2)$$

Rearrangement gives [10]

$$\frac{dV}{dI} = R_s + \frac{nkT}{q}\left(I+I_{sc}\right)^{-1}. \qquad (3)$$

From the results of the *I-V* measurement, we can obtain the plot of d*V*/d*I* vs $(I+I_{sc})^{-1}$. Figure 4 shows the plot of d*V*/d*I* vs $(I+I_{sc})^{-1}$ obtained from the results of the *I-V* measurement of the InGaP/InGaAs/Ge triple-junction cell (grid pitch: 120 μm). R_s was obtained from the intercept of this plot, and the R_s of the InGaP/InGaAs/Ge triple-junction solar cell was 0.025 Ω.

Moreover, we fabricated the triple-junction solar cells with various grid pitches, and evaluated R_s by the same method. Figure 5 shows the R_s values of the triple-junction solar cells with various grid pitches. R_s decreased with grid pitch. For concentrator cells, a reduction in R_s is necessary. However, when the grid pitch decreases, the number of grid electrodes increases, and shadow losses due to electrodes increase. Therefore, the optimization of the grid pitch, taking the trade-off of the R_s and shadow losses into consideration, is necessary. The optimization of the grid pitch is described in section 5.1.

3.2 Series resistance components

The series resistance of solar cells consists of various components. Figure 6 shows the various components of the series resistance of the InGaP/InGaAs/Ge triple-junction solar cell. The contact resistance was sufficiently reduced using the n-GaAs contact layer, as shown in Fig. 1. The resistances due to the InGaP layer, InGaAs layer and Ge substrate were considerably lower than the resistances such as electrode resistance (R_{SE}), tunnel junction resistances (R_{T1} and R_{T2}) and lateral resistance between electrodes (R_{SL}). Therefore, it is considered that R_{SE}, R_{SL}, R_{T1} and R_{T2} are the main components of R_s.

To obtain R_{SE}, the electrode was removed from the cell by etching the GaAs contact layer, as shown in Fig. 7. We measured the *I*-*V* characteristics of the electrode, as shown in Fig. 7, and the resistances (R_{SEall}) for various numbers (N) of grid electrodes were measured. R_{SEall} is given by

$$R_{SEall} = R_{SE}' \times 1/N + C, \quad (4)$$

where R_{SE}' and C are the resistance per grid electrode and a constant, respectively. R_{SE}' was estimated as the gradient by plotting $1/N$ vs R_{SEall} (Fig. 8). The estimated R_{SE}' was 2.96 Ω. In actual cell operations, the current is taken out from two pad electrodes. Therefore, R_{SE} is given by [9]

$$R_{SE} \quad R_{SE}' / 4N. \quad (5)$$

The number of grid electrodes in the triple-junction solar cell was 55. Therefore, the estimated R_{SE} was 0.0134 Ω.

The carriers that reach the emitter (*n*-type) layer of the InGaP junction have to move toward the electrodes through the AlInP window layer and the emitter layer of the InGaP junction. Therefore, R_{SL} was estimated from the sheet resistance (R_{sheet}) of the epitaxial layers in the AlInP window layer and the emitter layer of the InGaP junction. R_{SL} is given by

$$R_{SL} \quad R_{sheet} \times D/4N \times 0.7, \qquad (6)$$

where D is the grid pitch (cm), and 0.7 (cm) in eq. (6) is caused by the length of grid electrodes. The estimated R_{SL} was 0.0102 Ω.

R_{T1} and R_{T2} were estimated from the current density-voltage (J-V) curves of p-AlGaAs/n-InGaP and p-GaAs/n-GaAs tunnel junctions (Fig. 9). The structures (thickness of each layer, carrier concentration, and so forth) of the tunnel junctions measured in Fig. 9 have striking resemblance to those of each tunnel junction in the InGaP/InGaAs/Ge triple-junction solar cell. When the triple-junction solar cell is irradiated by light, the forward bias current flows in the tunnel junctions. Therefore, the series resistance components due to the tunnel junctions were estimated from the slope of the J-V curves of the tunnel junctions in the forward bias voltage region. In this study, the slope of the J-V curves of the tunnel junctions at the current of 500 suns of the triple-junction solar cell was adopted. The estimated R_{T1} and R_{T2} were 0.0012 Ω and 0.0008 Ω, respectively.

As shown above, the sum total value of the series resistance components R_{SE}, R_{SL}, R_{T1} and R_{T2} for the triple-junction solar cell with a grid pitch of 120 μm was 0.0256 Ω. This total value agreed well with R_s that was estimated from the intercept in the plots of dV/dI vs $(I+I_{sc})^{-1}$ described in section 3.1.

4. EQUIVALENT CIRCUIT CALCULATION FOR TRIPLE-JUNCTION SOLAR CELL WITH SPICE

Equivalent circuit calculation is very useful for the evaluation of solar cells. Various evaluations using equivalent circuits have been reported [11, 12]. In this study, equivalent circuit calculations were performed with SPICE.

Figure 10 shows a schematic of the equivalent circuit model that expresses triple-junction solar cells. As shown in Fig. 10, the equivalent circuit model is composed of

three diodes connected in series.

In the SPICE calculations, the diode equations for DC current are given by

$$I = I_{(forward)} - I_{(reverse)}, \tag{7}$$

$$I_{(forward)} = K_1 \cdot I_0 \left\{ \exp\left(\frac{qV}{n_D kT} \right) - 1 \right\} + K_2 \cdot I_{0R} \left\{ \exp\left(\frac{qV}{n_R kT} \right) - 1 \right\}, \tag{8}$$

$$I_{(reverse)} = I_{BV} \left\{ \exp\left(\frac{-q(V + BV)}{kT} \right) \right\}, \tag{9}$$

where K_1, K_2, I_0, I_{0R}, I_{BV}, n_D, n_R, and BV are the high-injection factor, generation factor, saturation current, recombination current parameter, reverse breakdown knee current, emission coefficient, emission coefficient for recombination current, and reverse breakdown knee voltage, respectively.

The top (InGaP), middle (InGaAs) and bottom (Ge) diodes shown in Fig. 10 were optimized to fit the measured value of the current-voltage (*I*-*V*) curves of single-junction (InGaP, GaAs and Ge) solar cells. The structures (thickness of each layer, carrier concentration, and so forth) of the single-junction solar cells have striking resemblance to those of each junction in the InGaP/InGaAs/Ge triple-junction solar cell. Fittings were carried out, focusing on I_0, n_D, I_{0R}, n_R and R_{sh} as parameters; these parameters were varied so that the calculated value fit the measured value. The parameters obtained by fitting were utilized for determining the composition of each diode in the equivalent circuit model.

The resistance R_{SEL} in Fig. 10 was obtained from the sum of the resistance due to electrodes (R_{SE}) and the lateral resistance between electrodes (R_{SL}). The resistances due to the tunnel junctions (R_{T1} and R_{T2}) were estimated from the *J*-*V* curves of the *p*-AlGaAs/*n*-InGaP and *p*-GaAs/*n*-GaAs tunnel junctions. The methods for the evaluation of R_{SE}, R_{SL}, R_{T1} and R_{T2} were described in detail in section 3.2.

The generated current (I_p) in the equivalent circuit model was estimated from the

normal photocurrent of each subcell for light of 1sun (The photocurrents from InGaP, InGaAs and Ge subcells for 1sun (100 mW/cm^2, AM1.5G) are designed to be 13.78, 15.74 and 20.60 mA/cm^2, respectively.).

It has already been confirmed that the calculated values of electrical characteristics, such as the fill factor (*FF*), V_{oc}, I_{sc} and η obtained by our simulation methods, replicated the experimental values faithfully [8, 9]. The information about the equivalent circuit calculation for triple-junction solar cells with SPICE is explained in more detail in the references [8, 9].

5. OPTIMIZATION OF SOLAR CELL'S STRUCTURE FOCUSING ON SERIES RESISTANCE

5.1 Grid electrode pitch

Figure 11 shows the estimated values of the series resistance components due to electrodes (R_{SE}), tunnel junctions (R_{T1} and R_{T1}) and lateral resistances between electrodes (R_{SL}) for various grid pitches of the InGaP/InGaAs/Ge triple-junction cell. The methods for the estimation of series resistance components were described in detail in section 3.2. The sums of R_{SE}, R_{SL}, R_{T1} and R_{T2} show the total series resistances (R_s). It was found that R_s decreased with grid pitch. In particular, R_{SL} decreased significantly with grid pitch. For concentrator cells, a reduction in R_s is necessary in order to avoid the decrease in *FF* due to energy loss with increasing current. However, the number of grid electrodes increases with decreasing grid pitch, and the shadow loss due to electrodes increases. Figure 11 also shows the grid pitch dependence of the shadow loss. The shadow loss increased with decreasing grid pitch. Therefore, we have to optimize the grid pitch by carefully considering the trade-off of the shadow loss and R_s.

We calculated the η of the triple-junction cell for various grid pitches, taking the

R_s and shadow loss into consideration by SPICE calculation described in section 4. Figure 12 shows the grid pitch dependences of η at 250 suns, 500 suns and 1000 suns. The optimized grid pitches for operations of 250 suns, 500 suns and 1000 suns were 175 μm, 130 μm and 100 μm, respectively. It was found that the maximum conversion efficiency of 39.5% could be attained using the grid pitch of 130 μm at the operation of 500 suns.

5.2 Electrode design

The InGaP/InGaAs/Ge triple-junction solar cell with the developed electrode design was fabricated. For comparison, the solar cells with the conventional electrode design and various grid pitches were fabricated and evaluated.

Figure 13 shows the conventional (a) and developed (b) electrode designs. When the grid pitches of (a) and (b) in Fig. 13 are the same, the area covered by the electrode (shadow loss) and the irradiation area are almost the same. The conventional electrode design extracts the current from two directions. On the other hand, the developed electrode design extracts the current from four directions.

Figure 14 shows the measured series resistance (R_s), estimated series resistance components due to electrodes (R_{SE}), tunnel junctions (R_{T1} and R_{T2}) and lateral resistances between electrodes (R_{SL}) for the conventional (grid pitches: 95 μm, 120 μm, 135 μm, 170 μm and 195 μm) and developed (grid pitch: 120 μm) electrode designs. The methods for the measurement of R_s and estimation of the series resistance components are described in detail in sections 3.1 and 3.2, respectively. It was found that, for the grid pitch of 120 μm, R_{SE} was greatly reduced and R_s was reduced to 0.011 Ω from 0.025 Ω by utilizing the developed electrode design. From Fig. 11, it is necessary to reduce the grid pitch to 50 μm in order to achieve 0.011 Ω. However, the shadow loss increases significantly for the grid pitch of 50 μm. The adoption of the developed electrode design enables the achievement of R_s = 0.011

Ω without increasing shadow loss.

5.3 Cell size

To decrease the energy loss due to R_s, it is important to use solar cells with a small short-circuit current. Thus, the characteristics of small triple-junction solar cells with a small I_{sc} were examined by SPICE calculation.

Figures 15(a) and (b) show the calculated fill factor (*FF*) and η of the InGaP/InGaAs/Ge triple-junction solar cell for various cell sizes under concentrated light. A small cell size result in a high *FF* and a high η at a high concentration ratio because of a low current. It was found that the η of 40% at 500 suns could be accomplished using the cell size of 4 mm x 4 mm. Moreover, we expect that the maximum η values of 40.5% at 1000 suns for 4 mm x 4 mm and 41% at 1500 suns for 1 mm x 1 mm will be accomplished.

However, the production of concentrator modules with small cells becomes more complex, and the total cost of a concentrator system increases. By considering these results, we can optimize the cell sizes for various lenses and various concentration ratios for high-efficiency, low-cost concentrator systems.

6. CONCLUSION

The R_s of the InGaP/InGaAs/Ge triple-junction solar cell was evaluated in detail. The R_s of the triple-junction solar cell with a grid pitch of 120 μm was 0.025 Ω. R_s decreased with grid pitch. Moreover, the series resistance components such as electrode resistance, tunnel junction resistance and lateral resistance between electrodes were estimated separately.

The optimization of cell designs was performed, focusing on series resistance by SPICE calculation. Grid electrode pitch was optimized. It was found that the maximum

conversion efficiency of 39.5% could be attained using the grid pitch of 130 μm at the operation of 500 suns. The use of the developed electrode design was suggested. It was found that R_s was reduced to 0.011 Ω from 0.025 Ω by utilizing the developed electrode design for the grid pitch of 120 μm. Cell size was optimized, and it was found that the maximum η values of 40.5% at 1000 suns for 4 mm x 4 mm and 41% at 1500 suns for 1 mm x 1 mm could be accomplished.

ACKNOWLEDGMENTS

This work was partially supported by the New Energy and Industrial Technology Development Organization under the Ministry of Economy, Trade and Industry, Japan.

REFERENCES

1) J.M. Olson, S.R. Kurtz and A.E. Kibbler: Appl. Phys. Lett. **56** (1990) 623.

2) T. Takamoto, T. Agui, E. Ikeda and H. Kurita: Proc. 28th IEEE Photovoltaic Specialists Conf., Anchorage, (2000) 976.

3) H.L. Cotal, D.R. Lillington, J.H. Ermer, R.R. King and N.H. Karam: Proc. 28th IEEE Photovoltaic Specialists Conf., Anchorage, (2000) 955.

4) A.W. Bett, F. Dimroth, G. Lange, M. Meusel, R. Beckert, M. Hein, S.V. Riesen and U. Schubert: Proc. 28th IEEE Photovoltaic Specialists Conf., Anchorage, (2000) 961.

5) C.J. Gelderloos, C. Assad, P.T. Balcewicz, A.V. Mason, J.S. Powe, T.J. Priest and J.A. Schwartz: Proc. 28th IEEE Photovoltaic Specialists Conf., Anchorage, (2000) 972.

6) M.J. O'Neill, A.J. McDanal, M.F. Piszczor, M.I. Eskenazi, P.A. Jones, C. Carrington, D.L. Edwards and H.W. Brandhorst: Proc. 28th IEEE Photovoltaic Specialists Conf., Anchorage,

(2000) 1135.

7) D.D. Krut, G.S. Glenn, B. Bailor, M. Takahashi, R.A. Sherif, D.R. Lillington and N.H. Karam: Proc. 28th IEEE Photovoltaic Specialists Conf., Anchorage, (2000) 1165.

8) K. Nishioka, T. Takamoto, W. Nakajima, T. Agui, M. Kaneiwa, Y. Uraoka and T. Fuyuki: Proc. 3rd World Conference on Photovoltaic Energy Conversion, (2003) 3P-C3-71.

9) K. Nishioka, T. Takamoto, T. Agui, M. Kaneiwa, Y. Uraoka and T. Fuyuki: Jpn. J. Appl. Phys. **43**, No. 3 (2004) 882.

10) J.R. Sites and P.H. Mauk: Solar Cells **27** (1989) 623.

11) Z. Ouennoughi and M. Chegaar: Solid-State Electron. **43** (1999) 1985.

12) J. Zhao, A Wang, P. P Altermatt and M. A. Green: Proc. 26th IEEE Photovoltaic Specialists Conf., Anaheim, (1997) 227.

Fig. 1. Schematic of InGaP/InGaAs/Ge triple-junction solar cell.

Fig. 2. External quantum efficiency of InGaP/InGaAs/Ge triple-junction solar cell.

Fig. 3. Electrode design for concentrator cell.

Fig. 4. Plot of dV/dI vs $(I+I_{sc})^{-1}$ for triple-junction solar cell with grid pitch of 120 μm.

Fig. 5. Measured R_s for triple-junction solar cells with various grid pitches.

Fig. 6. Various components of series resistance.

Fig. 7. Method of measuring electrode resistance.

Fig. 8. Plot of $1/N$ vs R_{SEall}.

Fig. 9. *J*-*V* characteristics of *p*-AlGaAs/*n*-InGaP and *p*-GaAs/*n*-GaAs tunnel junctions.

Fig. 10. Schematic of equivalent circuit model for triple-junction solar cell.

Fig. 11. Grid pitch dependences of series resistance components and shadow loss.

Fig. 12. Grid pitch dependences of conversion efficiencies at various concentration ratios.

Fig. 13. Electrode designs for concentrator cells: (a) conventional design and (b) developed design.

Fig. 14. R_s, R_{SE}, R_{SL} and $R_{T1}+R_{T2}$ for conventional (grid pitches: 95, 120, 135, 170 and 195 μm) and developed (grid pitch: 120 μm) electrode designs.

Fig. 15. Calculated *FF* and conversion efficiency of InGaP/InGaAs/Ge triple-junction solar cell for various cell sizes under concentrated light.

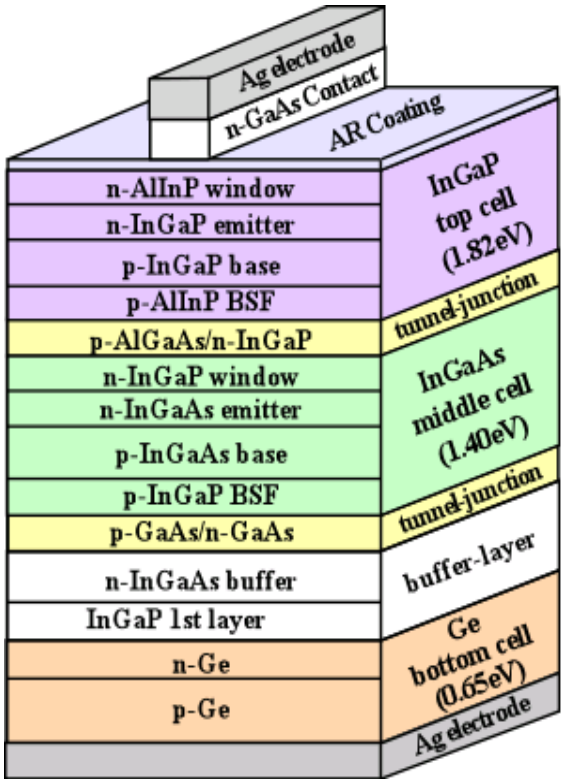

Fig. 1.

K. Nishioka

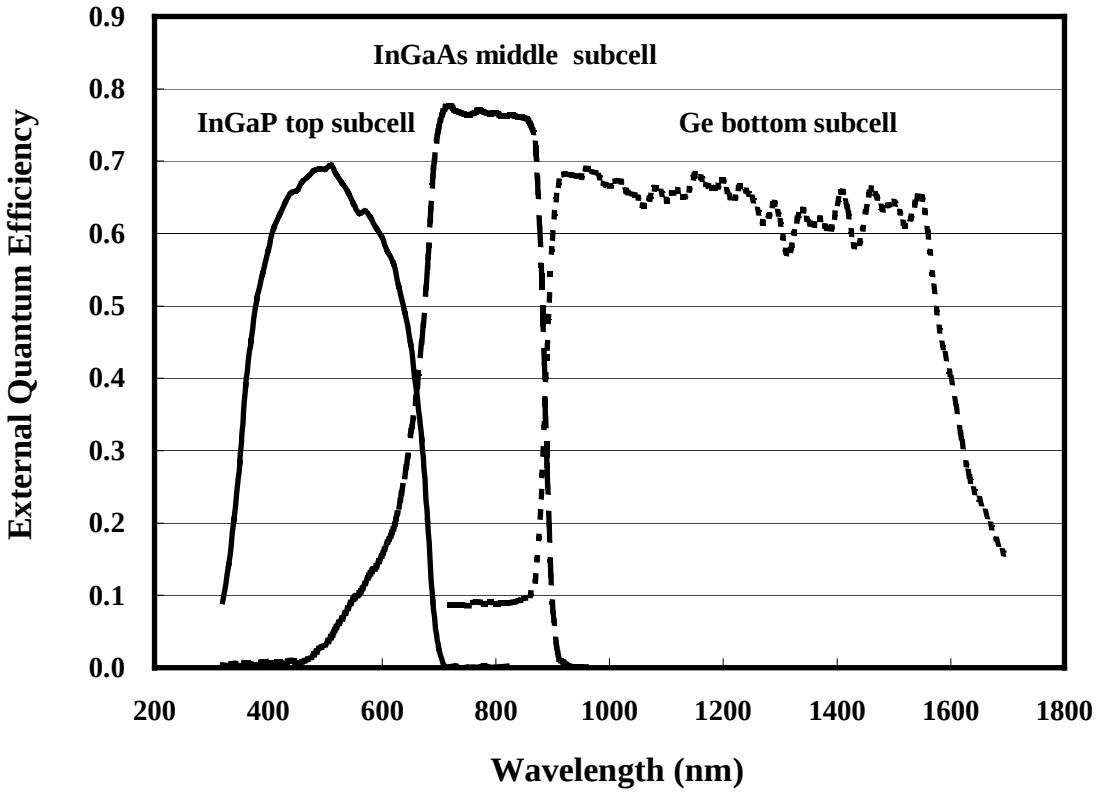

Fig. 2.

K. Nishioka

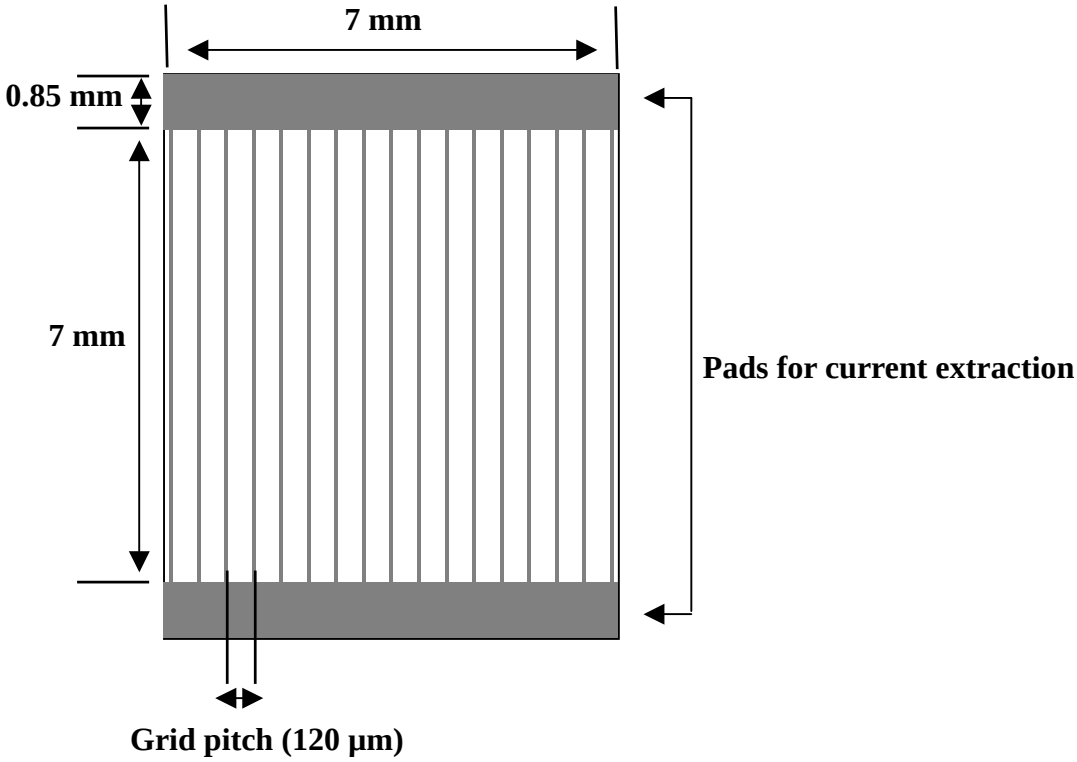

Fig. 3.

K. Nishioka

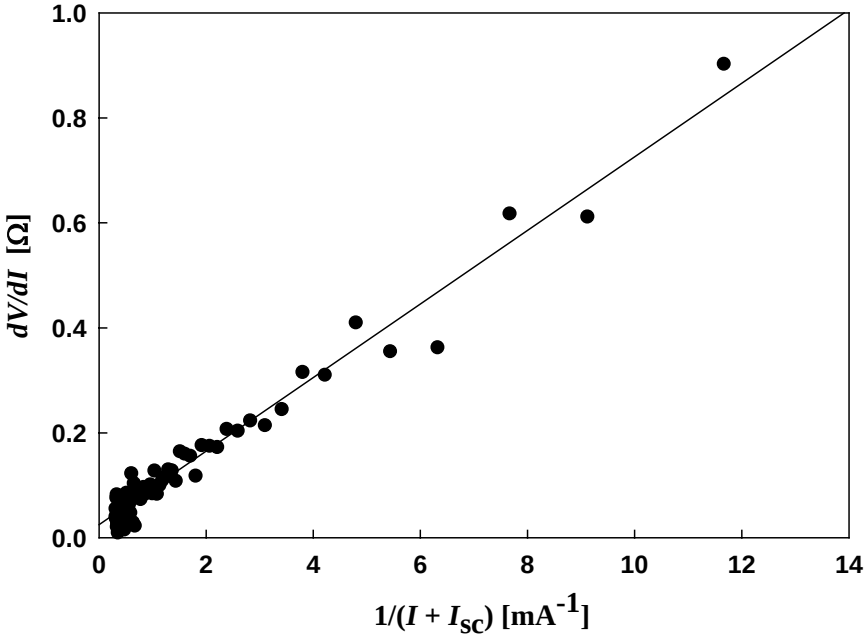

Fig. 4.

K. Nishioka

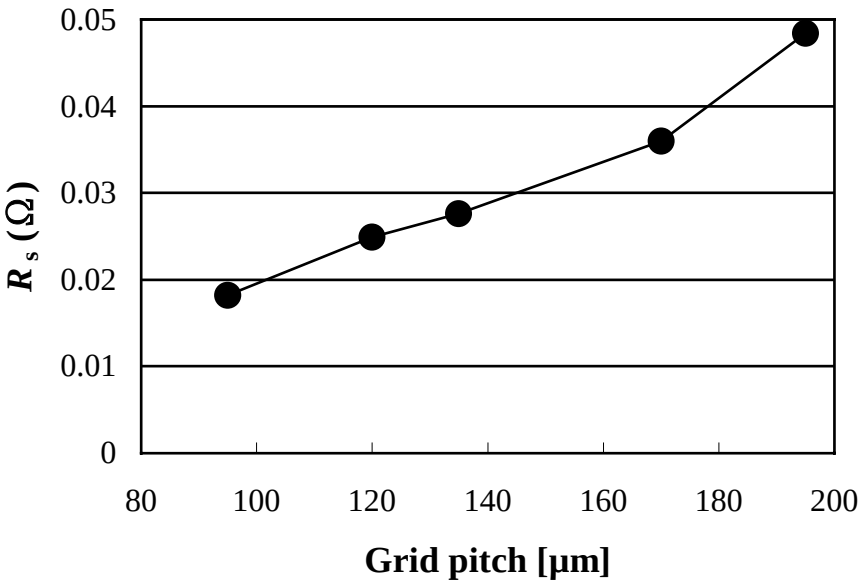

Fig. 5.

K. Nishioka

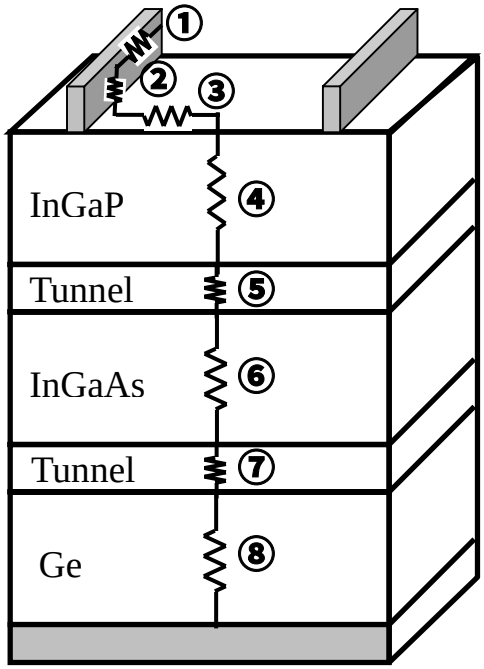

① Electrode resistance (R_{SE})
② Contact resistance
③ Lateral resistance (R_{SL})
④ Layer (InGaP) resistance
⑤ Tunnel resistance (R_{T1})
⑥ Layer (InGaAs) resistance
⑦ Tunnel resistance (R_{T2})
⑧ Ge substrate resistance

Fig. 6.

K. Nishioka

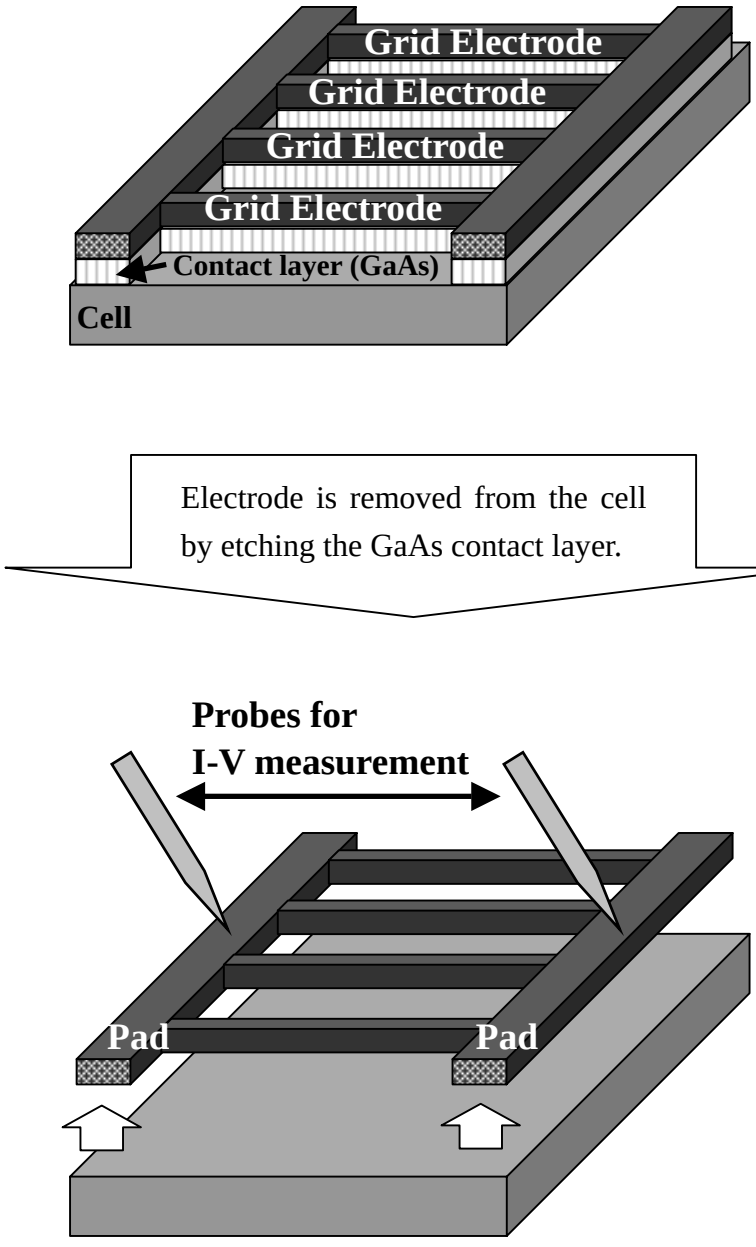

Fig. 7.

K. Nishioka

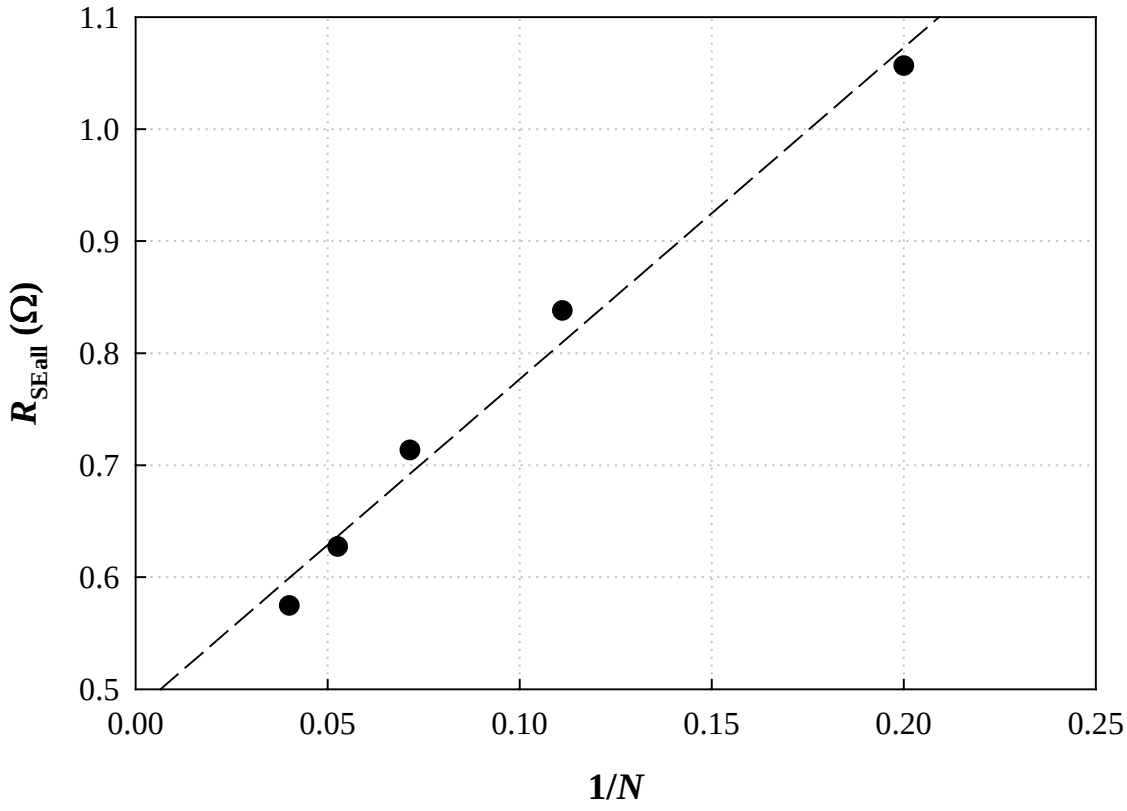

Fig. 8.

K. Nishioka

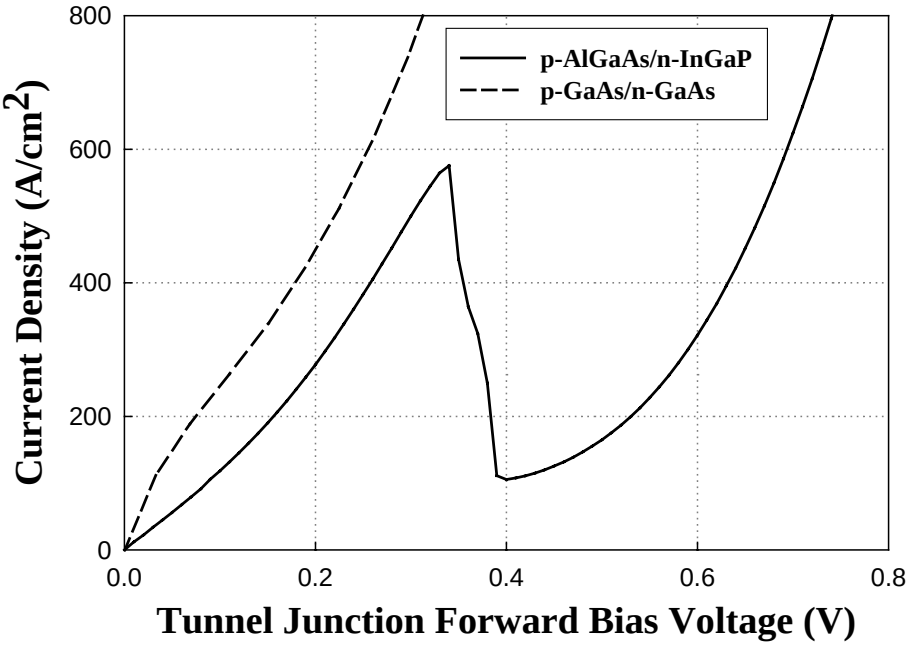

Fig. 9.

K. Nishioka

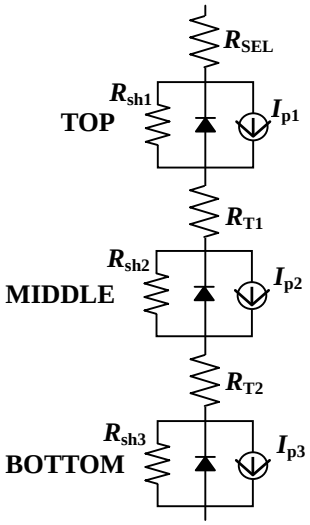

Fig. 10.

K. Nishioka

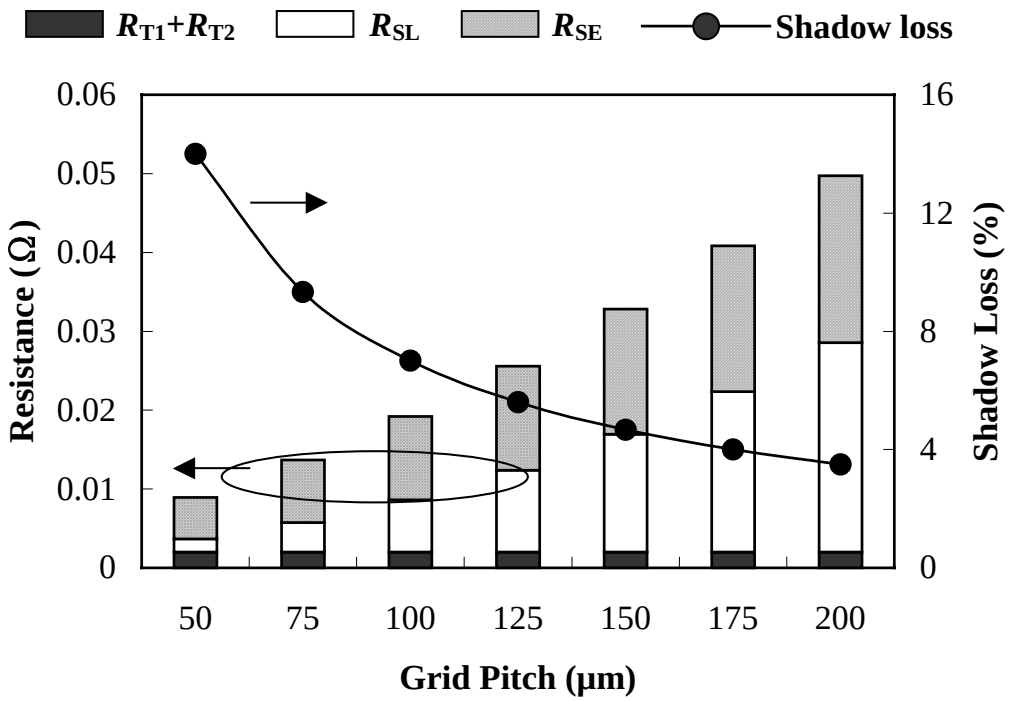

Fig. 11.

K. Nishioka

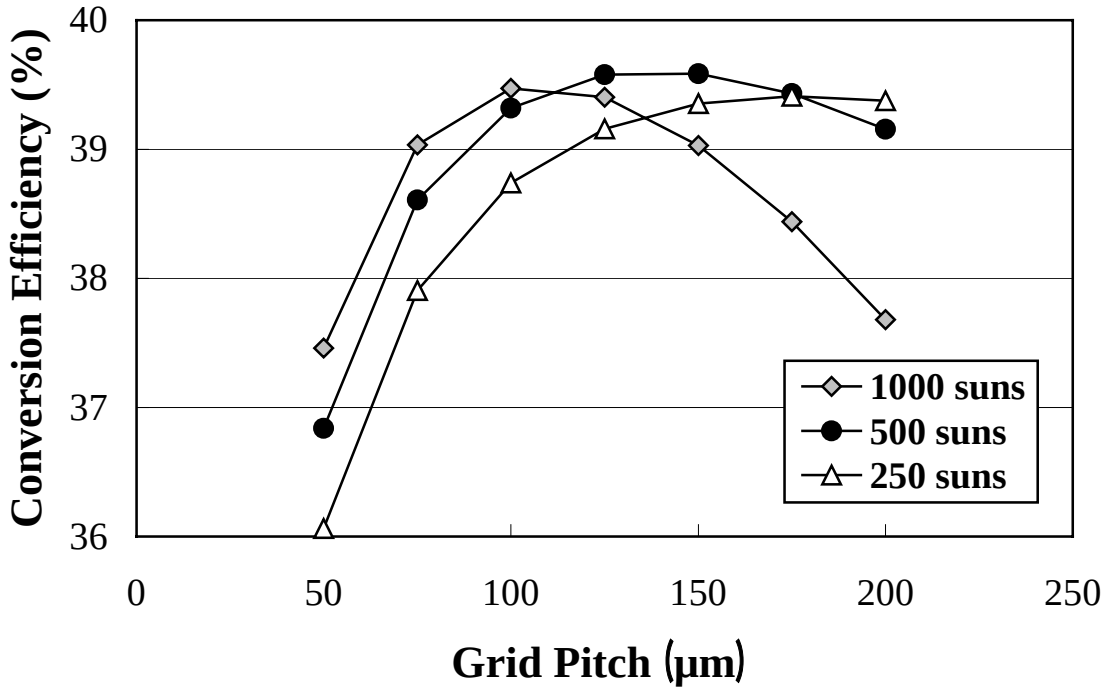

Fig. 12.

K. Nishioka

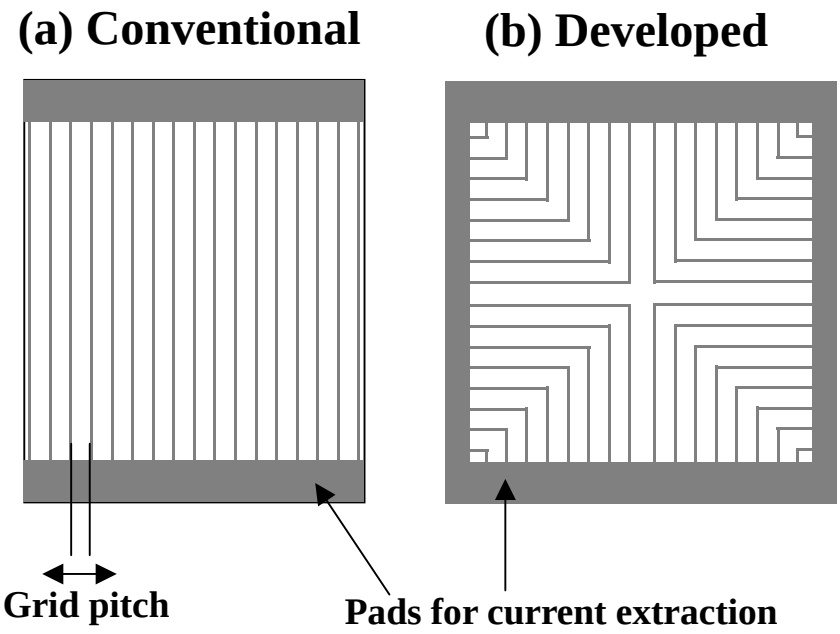

Fig. 13.

K. Nishioka

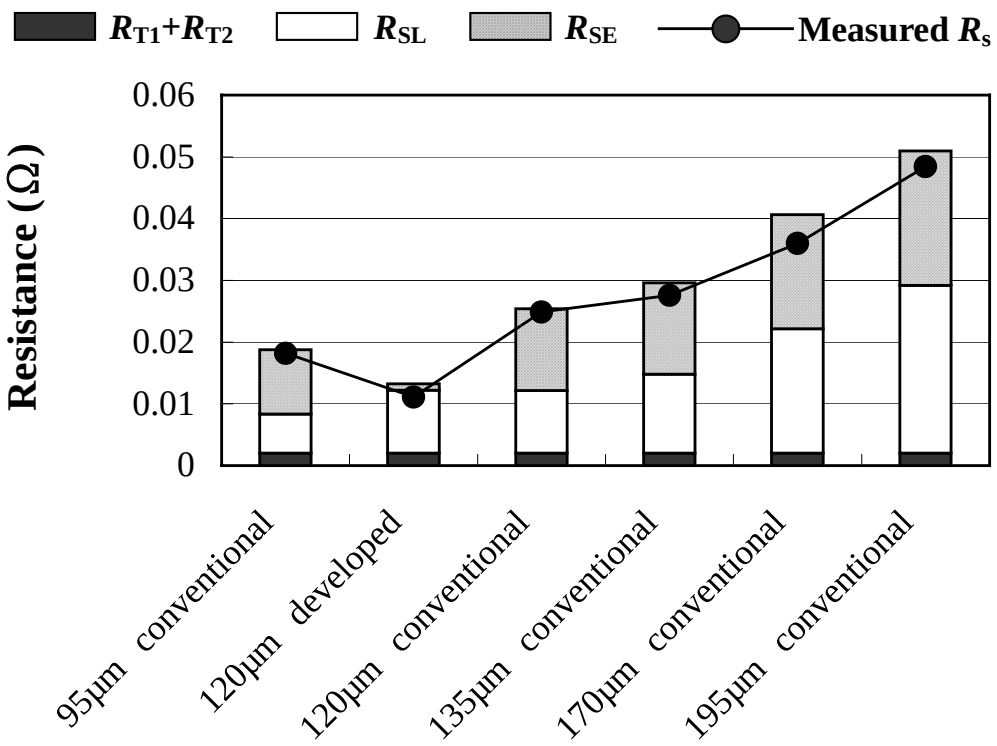

Fig. 14.

K. Nishioka

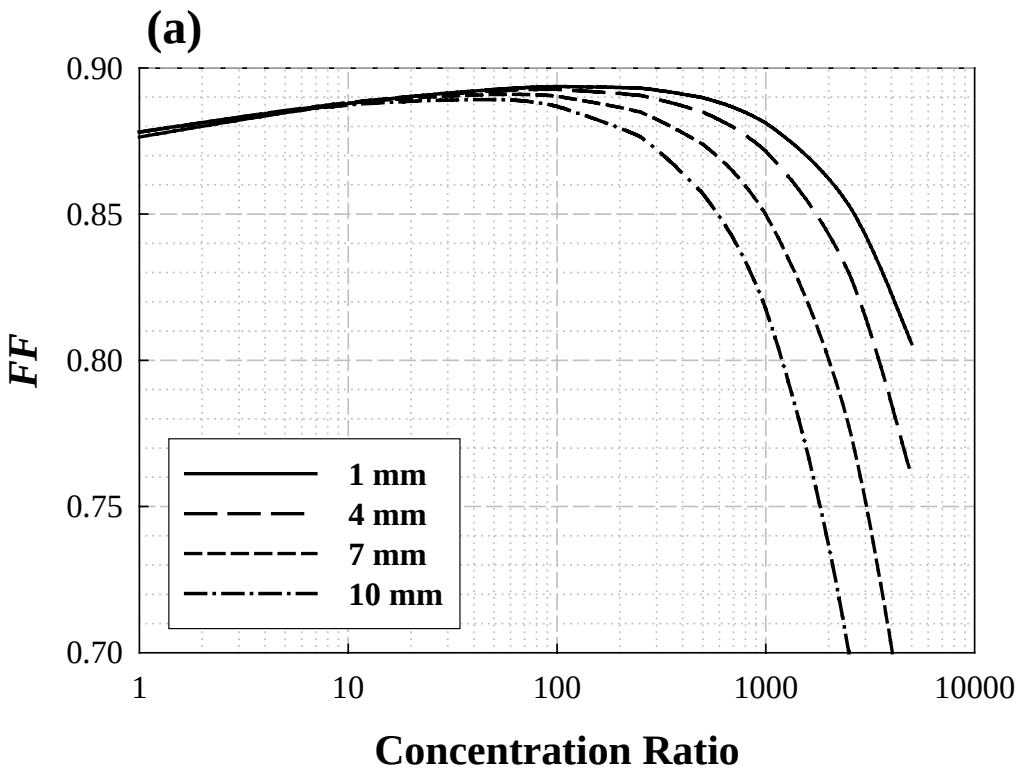

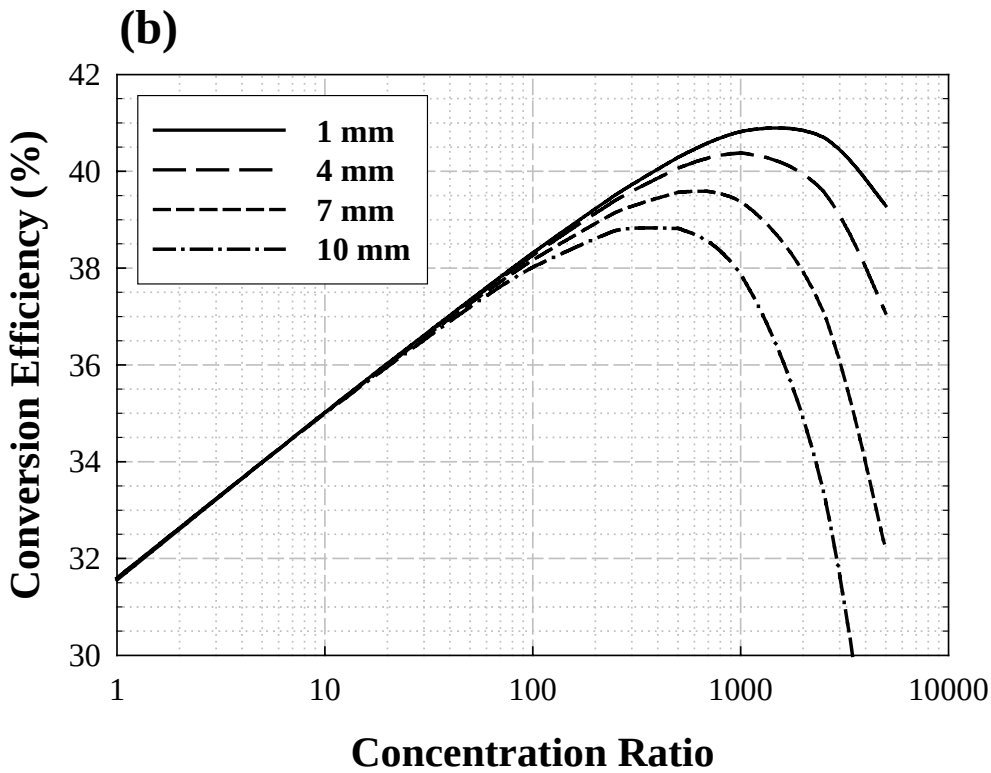

Fig. 15.

K. Nishioka